U.S. Department of Commerce
National Oceanic and Atmospheric Administration
National Weather Service
National Centers for Environmental Prediction
5830 University Research Court
College Park, MD 20740-3818

Office Note 505
https://doi.org/10.25923/cybh-w893

Updates in the NCEP GFS Cumulus Convection, Vertical Turbulent Mixing, and Surface Layer Physics

Jongil Han[1,3], Wei Li[2], Fanglin Yang[3], Edward Strobach[2], Weizhong Zheng[2], and Ruiyu Sun[2]

[1]Systems Research Group, Inc.
Environmental Modeling Center
National Centers for Environmental Predictions
College Park, Maryland

[2]I.M. Systems Group, Inc.
Environmental Modeling Center
National Centers for Environmental Predictions
College Park, Maryland

[3]Environmental Modeling Center
National Centers for Environmental Predictions
College Park, Maryland

Author E-mail: Jongil.Han@noaa.gov

Abstract

Significant model physics updates to cumulus convection, vertical turbulent mixing and surface layer physics were made, all of which represent candidate changes for the next version of the NCEP GFS. The updates aim mainly to enhance the underestimated surface-based convective available potential energy, to reduce the tropospheric cold temperature biases and the planetary boundary layer (PBL) dry moisture biases over the Tropics, to reduce the excessive vertical turbulence mixing in strong shear environment as well as the excessive PBL growth, to better predict the surface inversion as well as the capping inversion near the PBL top, to reduce the nighttime cold and daytime warm 2m temperature biases over forested regions, and to better represent sub-grid scale turbulence variability in the surface layer. The updated physics not only showed a significant improvement in 500-hPa height anomaly correlations, especially for a forecast lead time of 48-96-h and in the tropical wind vector root mean square errors, but it also improved a Madden-Julian Oscillation intensity and propagation especially for longer lead time.

1. Introduction

To reduce systematic or longstanding model biases, the model physics in the National Centers for Environmental Prediction's (NCEP) Global Forecast System (GFS) is under continuous development (e.g., Han and Pan, 2011; Han et al., 2016; Han et al, 2017; Han and Bretherton, 2019). The reduced biases are expected to result in an improvement of forecast performance.

The current operational NCEP GFS as of September 2021 (GFSv16) has longstanding biases of underestimated surface-based convective available potential energy (CAPE) and cold biases of tropospheric temperature profile. In addition, the GFS often experiences excessive cold (warm) biases in 2-m temperature during the nighttime (daytime) over forest regions. It has also been reported that the GFS often forecasts too weak of a nighttime surface inversion and overestimates the daytime planetary boundary layer (PBL) growth.

In this study we update the GFS cumulus convection, PBL and surface layer physics to not only reduce model biases previously mentioned, but also to include missing physics in the GFS. Details of the updates and new parameterizations are described in Section 2. In Section 3 we evaluate the impacts of the updates on medium-range forecasts and the prediction of the Madden-Julian Oscillation (MJO) for a particular case. Finally, in Section 4 we summarize our study.

2. Updates in model physics

2.1. Update in cumulus convection

One of the long-standing model biases in the GFS is a large underestimation of the surface-based convective available potential energy (CAPE) (EMC Model Evaluation Group [MEG] presentation, 2020). The underestimation of the CAPE would be attributed to many factors such as underestimated soil moisture. Since cumulus convection always stabilizes the environment when triggered, then stronger convection would reduce CAPE even more. To enhance the CAPE in this study, we apply stricter convection triggering conditions. Firstly, if the sub-cloud mean relative humidity (RH) is less than a threshold value (currently set to 75%), convection is not triggered. Secondly, the ascent of a surface updraft parcel lifted from the model first layer now starts from the lower 20% of PBL depth only for convection triggering condition check, but once convection is triggered, the mass-flux transport starts from the model first layer. This helps to avoid a spurious convection triggering due to rapid surface heating in the morning. Thirdly, separation cloud depth of deep and shallow convection is increased to 200 hPa from 150 hPa. It could reduce the occurrence of deep convection while increasing that of shallow convection and consequently, would increase the CAPE.

Another systematic bias in the GFS is a cold bias in tropospheric temperature profile, especially over the Tropics. To reduce this cold bias, the convective rain evaporation is reduced with removal of wind shear dependency. In the update, in addition, the entrainment rate below cloud base is reduced by 30 %, which helps to reduce false alarm storms in the GFS. The last modification is an adjustment to the starting point of enhanced downdraft detrainments from cloud base to 60 hPa above

ground surface. We justify this modification since downdraft detrainments starting from relatively high cloud bases are unrealistic, as is the case in the current version of the GFS.

Fig. 1 shows that the CAPE is largely enhanced, especially over the Tropics, mainly due to stricter convective triggers. However, the CAPE enhancement over the continental United States (CONUS) is small. It indicates that further improvement in model physics is needed to enhance the CAPE over mid-latitude land areas. Fig. 2 displays that the reduced convective rain evaporation significantly reduces the cold bias in tropospheric temperature profile over the Tropics compared to the Radiosonde observations.

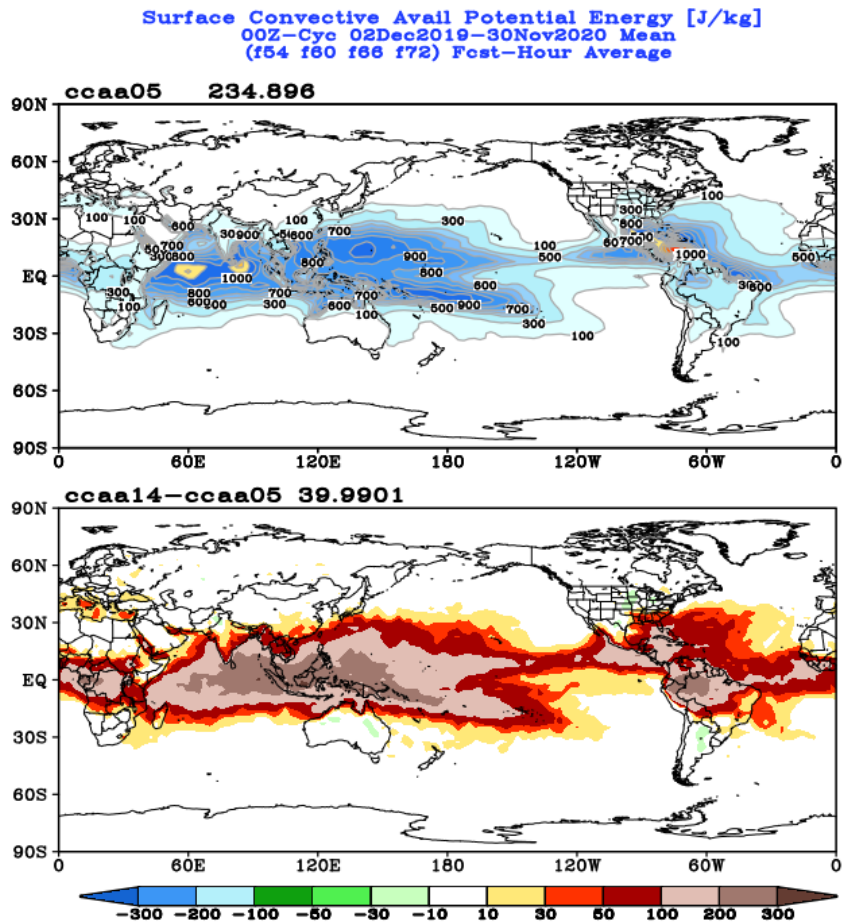

Fig. 1. Mean surface-based CAPE from the control run (ccaa05; upper panel) and the mean CAPE difference (ccaa14-ccaa05; lower panel) between the experimental run with stricter convection trigger conditions (ccaa14) and the control run.

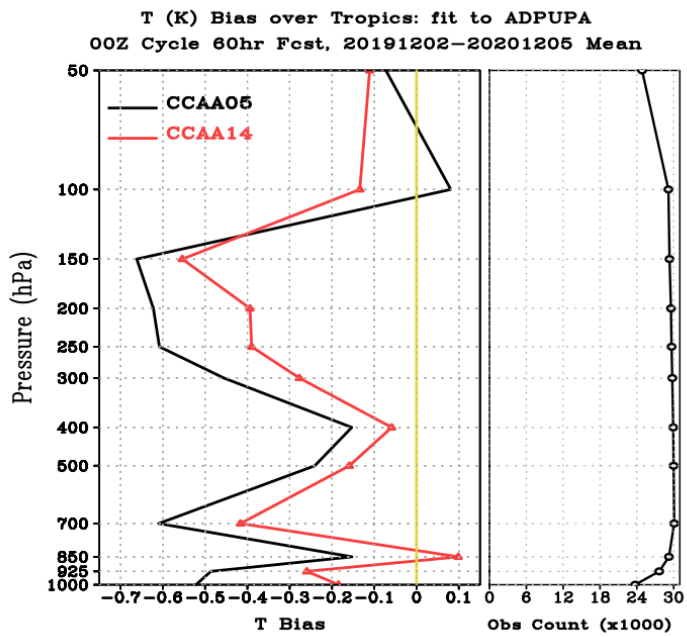

Fig. 2. Mean temperature vertical profile biases over Tropics at 60 forecast hours from the control run (CCAA05) and the experimental run with reduced rain evaporation (CCAA14), compared to the Radiosonde observations.

2.2. Update in vertical turbulent mixing

The turbulent mixing length, l_k, in the GFS vertical turbulent mixing scheme (Han and Bretherton, 2019) is defined by the harmonic average of the surface layer length scale (l_1) and a characteristic length scale (l_2), i.e.,

$$\frac{1}{l_k} = \frac{1}{l_1} + \frac{1}{l_2} \tag{1}$$

Following Bougeault and Lacarrere (1989), l_2 is given by

$$l_2 = \min\left(l_{up}, l_{down}\right) \tag{2}$$

where l_{up} and l_{down} are the distances that a parcel having an initial TKE can travel upward and downward before being stopped by buoyancy effects, both of which are represented by

$$\int_z^{z+l_{up}} \frac{g}{\overline{\theta}_v}\left(\overline{\theta}_v(z) - \overline{\theta}_v(z')\right)dz' = \overline{e}(z) \quad \text{and} \quad \int_{z-l_{down}}^{z} \frac{g}{\overline{\theta}_v}\left(\overline{\theta}_v(z') - \overline{\theta}_v(z)\right)dz' = \overline{e}(z), \tag{3}$$

where e is the turbulent kinetic energy (TKE); θ_v is the virtual potential temperature and g is gravity. Eq. (3) considers only buoyancy and tends to overestimate the mixing length

(Rodier et al., 2017). In a neutral atmosphere, Eq. (3) indicates that the mixing length can be infinite, which is physically not acceptable. Based on excessively large mixing lengths calculated from Eq. (3), we adopt a wind shear effect in the mixing length calculation following Rodier et. al. (2017) as:

$$\int_{z}^{z+l_{up}} \left[\frac{g}{\overline{\theta}_v} \left(\overline{\theta}_v(z) - \overline{\theta}_v(z') \right) + C_0 \sqrt{e} S(z') \right] dz' = \overline{e}(z) \quad \text{and}$$

$$\int_{z-l_{down}}^{z} \left[\frac{g}{\overline{\theta}_v} \left(\overline{\theta}_v(z') - \overline{\theta}_v(z) \right) + C_0 \sqrt{e} S(z') \right] dz' = \overline{e}(z), \tag{4}$$

where C_0 is a constant and S(z′) is the local vertical wind shear. Eq. (4) can reduce the mixing length in strongly sheared environments such as that seen in hurricanes, which leads to a reduction of the turbulent eddy diffusivity. Fig. 3 shows that reducing the mixing length via Eq. (4) enhances the hurricane intensity due to weakened turbulence mixing, leading to better agreement of storm intensity with observations.

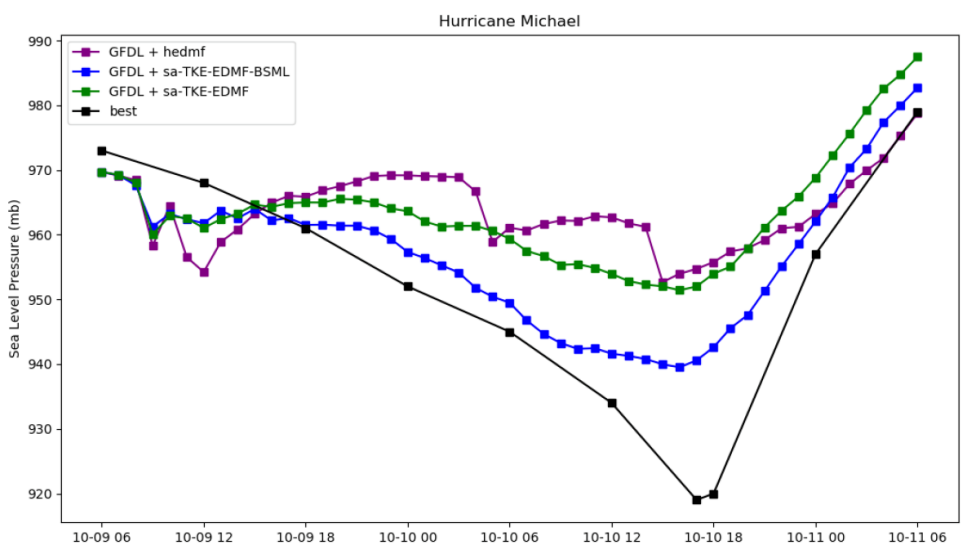

Fig. 3. Mean sea level pressure evolution of 2018 hurricane Michael for the control run (green line) and the experimental run with the reduced mixing length (blue line), compared to observation (black line).

In the current operational GFS, the background diffusivity ($K_0[m^2s^{-1}]$) and background characteristic mixing length ($l_0[m]$) exponentially decrease with height, and are given by

$$K_0 = 1.0e^{\left[-10(1-P/P_s)^2\right]}, \qquad l_0 = 30.0e^{\left[-2.5(1-P/P_s)^2\right]}, \tag{5}$$

where P is the layer pressure and P_s is the surface pressure. The GFS often underestimates the surface inversion due to too large K_0 and l_0 in the inversion layers. To better predict the surface and capping inversions, K_0 and l_0 in the inversion layers are

reduced as a function of surface momentum roughness length ($z_0[m]$) and green vegetation fraction (σ_f). Revisions to K_0 and l_0 in the inversion layers above 250 m are given by

$$K_0=\min(K_0, 0.15) \text{ and } l_0=\min(l_0, 5), \tag{6}$$

whereas K_0 and l_0 in the inversion layers below 250 m are given by

$$K_0'=K_0\times F \text{ and } l_0'=l_0\times F,$$
$$K_0=\min(\max(K_0', 0.3), K_0) \text{ and } l_0=\min(\max(l_0', 10), l_0), \tag{7}$$

where

$$F=\sqrt{f(z_0)f(\sigma_f)}, \qquad f(z_0)=\frac{(z_0-0.1)}{0.9}, \qquad f(\sigma_f)=\max(\sigma_f, 0.1). \tag{8}$$

In Eq. (8), $f(z_0) = 0$ for $z_0 < 0.1$ m and $f(z_0) = 1$ for $z_0 > 1.0$ m. Fig. 4 shows that the reduced K_0 and l_0 in the inversion layers improve the surface inversion prediction especially over areas with smaller z_0 and σ_f.

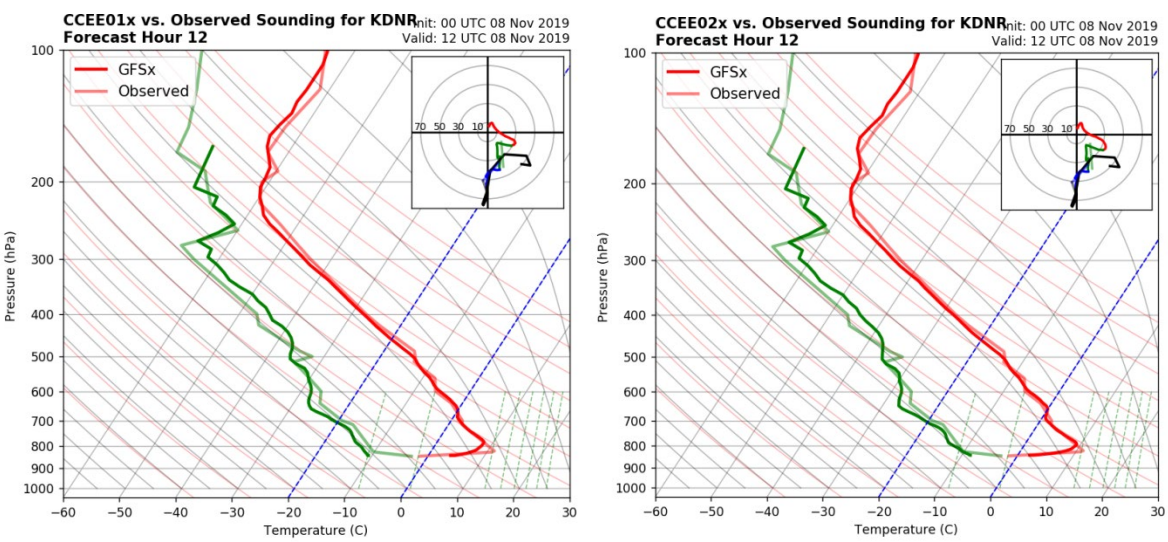

Fig. 4. Vertical profiles of temperature (red lines) and dew-point temperature (green lines) at a station at Denver, Colorado, at 12 forecast hours. Dark color lines are from the model forecasts and light color lines are from the observations. Left and right panels display the results from the control run (CCEE01x) and the experimental run with the reduced background diffusivity and mixing length in the inversion layers (CCEE02x), respectively.

In the current operational GFS, the daytime PBL height h is determined by the height of w_u=0, where w_u is the updraft parcel velocity. We have found that the PBL height is often overestimated due to too much overshoot of the updraft parcel. To suppress too much PBL growth, the PBL updraft overshoot is limited by bulk Richardson number-based-PBL depth as in Han and Bretherton (2019).

2.3. Update in surface layer physics

a) New canopy heat storage parameterization

Over forested regions, the GFS often experiences excessive cold and warm biases during the night- and daytime in 2-m temperature, respectively. The excessive cold and warm 2-m temperature biases in GFS over forested regions could be due to a lack of heat storage in the GFS surface layer model over land. Heat storage for a tall forest can reach several tens of Wm^{-2} under extreme conditions (Garratt, 1992) and can reduce the diurnal variation of near-surface temperature.

According to Heidkamp et al. (2018), the canopy heat storage is composed of the heat storage in the canopy air space (~19%), the heat storage of biomass (~60%), and the latent heat storage (~22%). In this study we propose a simple parameterization of heat storage in forest canopies. The new canopy heat storage parameterization (CHSP) is achieved by reducing the input sensible heat flux as surface boundary forcing into the PBL scheme as a function of surface roughness and vegetation fraction.

Fig. 5 displays the new CHSP schematically. During daytime, a portion of the surface sensible heat flux (H_s) is stored within the canopy layer and the remaining sensible heat flux (H_1) enters the PBL, thus resulting in a positive heat storage (i.e., $\Delta H = H_s - H_1 > 0$). Conversely, during nighttime, the downward sensible heat flux into the ground surface (H_s) is larger than the sensible heat flux entering from the PBL into the canopy layer (H_1), thus resulting in a negative heat storage (i.e., $\Delta H = H_s - H_1 < 0$). Note that the current CHSP has no impact on the surface energy budget equation.

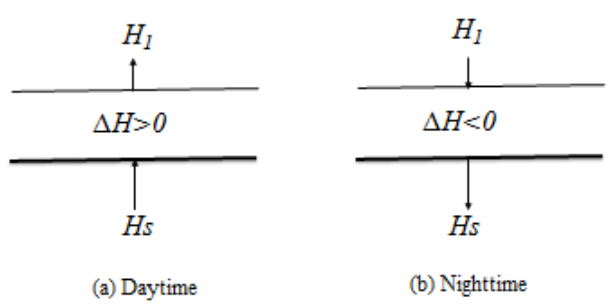

Fig. 5. Schematic diagram for the new CHSP, where H_s is the sensible heat flux at the ground surface, H_1 is the sensible heat flux at the top of the canopy layer, and $\Delta H = H_s - H_1$ is the heat flux stored within the canopy layer.

In the new CHSP, H_1 is given by

$$H_1 = \frac{H_s}{\left[1 + a_1 F\right]} \tag{9}$$

where F is defined in Eq. (8) and α is the empirical coefficient. We set a_1=0.25 for unstable conditions during daytime, while a_1=1.0 is used for stable conditions during nighttime.

Fig. 6 displays the diurnal variation of 2-m temperature over equatorial regions in Africa where the mean roughness length is about 0.95 m and the mean green vegetation fraction is about 64 %. As expected, the CHSP reduces the diurnal variation of 2-m temperature by reducing daytime temperature and increasing nighttime temperature.

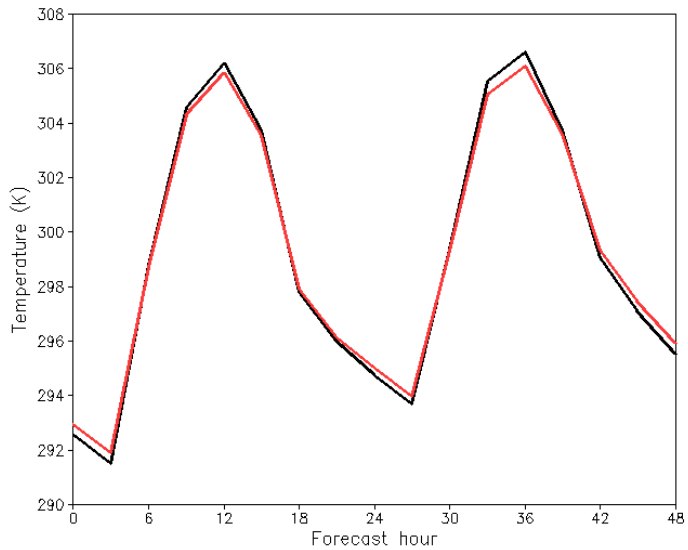

Fig. 6. Diurnal variation of 2-m temperature for the control run (black) and the run with the new CHSP (red), averaged over equator regions in Africa (0-5oN, 30-35oE) where the mean roughness length is about 0.95 m and the mean green vegetation fraction is about 64 %.

b) Inclusion of sea spray effect parameterization

Under high-wind conditions such as in hurricanes, breaking ocean waves eject sea spray droplets into the atmosphere. The near-surface atmospheric layers would have additional sensible and latent heat fluxes from the ejected spray droplets which have the same temperature and salinity as that on the ocean surface. Based on studies from Fairall et al. (1994) and Andreas et al. (2008), the total sensible ($H_{S,T}$) and latent ($H_{L,T}$) heat fluxes over ocean are given by

$$H_{L,T} = H_L + \alpha Q_L, \qquad H_{S,T} = H_S + \beta Q_S - (\alpha - \gamma) Q_L, \tag{10}$$

where H_L and H_S are latent and sensible heat fluxes from the ocean surface, respectively, Q_L and Q_S are latent and sensible heat fluxes from the spray droplets, respectively, and α

and β are tunable empirical coefficients set to $\alpha=\beta=0.75$ in this study (Fairall et al. [1994] set $\alpha=\beta=0.5$). The γ is also a tunable empirical coefficient representing the effect of spray droplets going back to sea (Andreas et al., 2008) and set to $\gamma=0.2$ in this study.

Following Fairall et al. (1994), the Q_L and Q_S are given by

$$\begin{aligned} Q_L &= 7.2\times10^{-9} u_{10}^{5.4} A(u_{10}) B(T_a) \rho_a L_v [q_s(T_a) - q], \\ Q_S &= 6.4\times10^{-8} u_{10}^{3.4} A(u_{10}) \rho_a C_{pa} (T_s - T_a). \end{aligned} \tag{11}$$

Here, u_{10} is the wind speed at 10-m above the sea surface, ρ_a the air density in the atmospheric surface layer, C_{pa} the specific heat of air at constant pressure, L_v the latent heat of condensation, q_s the saturation specific humidity, T_s the sea surface temperature, and T_a and q are air temperature and specific humidity in the atmospheric surface layer. The terms, $A(u_{10})$ and $B(T_a)$ are given by

$$A(u_{10}) = 1 - 0.087 \ln\left(\frac{10}{0.015 u_{10}}\right), \qquad B(T_a) = \left[1 + \frac{0.622 L_v^2}{R C_{pa} T_a^2} q_s(T_a)\right]^{-1}. \tag{12}$$

where R is the gas constant of dry air. Eqs. (10) and (11) indicate that the sea spray effect parameterization enhances sensible and latent heat fluxes, especially for strong wind conditions such as hurricanes, and thus enhances the intensity of hurricane forecasts.

c) Inclusion of molecular viscosity effect in momentum roughness length (z_0) computation over ocean

In the current operational GFS, the momentum roughness length (z_0) over ocean is calculated by Charnock's relation (1955), that is,

$$z_0 = 0.014 \frac{u_*^2}{g} \tag{13}$$

where u_* is the friction velocity. To reduce drag in high wind conditions (e.g., 10-m wind speeds greater than 30 m/s), z_0 is limited to the value of 0.317×10^{-2} [i.e., $z_0=\min(z_0, 0.317\times10^{-2})$].

Eq. (13) tends to underestimate z_0 especially in weak wind conditions due to lack of molecular viscosity effect. Following Smith (1988) and Beljaars (1994), we include the molecular viscosity effect in z_0 computation with a slightly increased empirical coefficient in Eq. (13) as

$$z_0 = 0.11 \frac{\nu}{u_*} + 0.018 \frac{u_*^2}{g}, \tag{14}$$

where ν is the molecular viscosity of air. As shown in Fig. 7, the combined updates in the effect of sea spray and adjustments to z_0 reduce the dry bias in the PBL over the tropical ocean by enhancing the latent heat flux over the ocean. This was also found to positively impact MJO prediction (not shown).

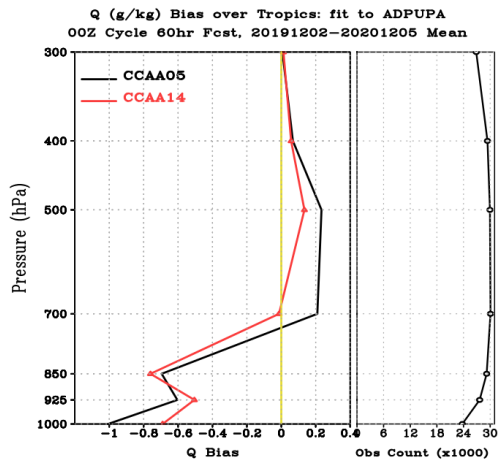

Fig. 7. Mean specific humidity vertical profile biases over Tropics at 60 forecast hours from the control run (CCAA05) and the experimental run with the sea spray effect parameterization and molecular viscosity effect in momentum roughness length computation over ocean (CCAA14), compared to the Radiosonde observations.

d) Thermal roughness length modification over land

Zilitinkevich (1995) relates the thermal roughness length (z_t) to z_0 as a function of atmospheric flow; that is,

$$z_t = z_0 \exp\left(-\kappa C_{zil}\sqrt{u_* z_0/\nu}\right) \tag{15}$$

where $\kappa = 0.4$ is the von Karman constant and C_{zil} is an empirical coefficient. Zheng et al. (2012) modified Eq. (15) with the inclusion of a vegetation fraction effect as

$$z_t = z_0 \exp\left(-\kappa C_{zil}\left[1-\sigma_f\right]^2\sqrt{u_* z_{0g}/\nu}\right) \tag{16}$$

where z_{0g} is the bare soil momentum roughness length (taken as 0.01 m) and C_{zil} is set to 0.8. Eq. (16) is used in the current operational GFS.

In the modified version, the constant, z_{0g}, is replaced with the original z_0 from Zilitinkevich (1995) while C_{zil} is treated as a function of z_0 rather than a constant, based on studies by Trier et al. (2011) and Chen and Zhang's (2009); that is,

$$z_t = z_0 \exp\left(-\kappa C_{zil}(z_0)\left[1-\sigma_f\right]^2\sqrt{u_* z_0/\nu}\right), \qquad C_{zil}(z_0) = 10^{-4.0 z_0}. \tag{17}$$

In this study, $C_{zil}(z_0)$ is set to range within 0.08-0.8. While Eq. (17) produces z_t values similar to those from Eq. (16), it appears to be more physically justifiable.

e) New parameterization of maximum *z/L* [$(z/L)_{max}$] in the stable surface layers

In very stable conditions, the surface layer stability parameter *z/L* (where *L* is the Monin-Obukhov length) can be very large and as a result, a numerical weather forecast model can produce unrealistically cold 2-m temperatures due to a decoupling from the ground surface. In reality, *z/L* cannot be infinitely large, and is limited to a value [$(z/L)_{max}$] due to a sub-grid scale turbulence variability.

Zheng et al. (2017) set to $z/L < [(z/L)_{max} = (z/L)_{crit}]$ in the GFS surface layer scheme, where $(z/L)_{crit}$ is a critical *z/L* for turbulence collapse as a function of surface momentum roughness length z_0, defined as (van de Wiel et al., 2007),

$$\left(\frac{z}{L}\right)_{crit} = \frac{\ln\left(z / z_0\right)}{10\left(1 - z_0 / z\right)} \tag{18}$$

Note that Eq. (18) does not represent sub-grid scale turbulence variability, but is a threshold *z/L* separating a continuously turbulent stationary flow from collapsed turbulence. Therefore, setting $(z/L)_{max} = (z/L)_{crit}$ is not physically justifiable, although it may help to reduce cold 2m temperature bias in forested regions during nighttime.

In this study we develop a new parameterization for the $(z/L)_{max}$. The *z/L* is defined as

$$\frac{z}{L} = -\frac{\kappa\left(g / T\right)\left(H_s / \rho_a C_{pa}\right)}{u_*^3} \tag{19}$$

Considering that

$$\frac{H_0}{\rho c_p} = K\frac{\partial\theta}{\partial z} \qquad \text{and} \qquad u_*^2 = K\frac{\partial U}{\partial z} \tag{20}$$

where *K* is the turbulent eddy diffusivity. Substituting Eq. (20) into Eq. (19) gives rise to

$$\frac{z}{L} = \left(\frac{g}{T}\right)\left[\frac{(\theta_v - \theta_{v0})z^{1.5}}{U^{1.5}}\right]\left(\frac{1}{\sqrt{K}}\right) \tag{21}$$

Eq. (21) can lead to a parameterization of $(z/L)_{max}$ as

$$\left(\frac{z}{L}\right)_{\max} = \sqrt{\frac{K_{ref}}{K_0}} \tag{22}$$

where K_{ref} is a reference tunable constant background diffusivity, currently set to 0.09. Eq. (22) indicates that $(z/L)_{max}$ is inversely proportional to the square root of the background diffusivity, K_0. Since K_0 represents a sub-grid scale turbulence variability, Eq. (22) is a physically plausible assumption.

3. Results for medium-range forecasts and a Madden-Julian Oscillation (MJO) case prediction

To assess the impacts of revised physics described in section 2 on medium-range forecast skill, 6-day forecasts at 00Z cycle every 5 days were conducted for the period of December 2, 2019 – December 1, 2020 using initial conditions from the GFSv16 (which is the same as the current operational GFS) parallel runs. The GFS used in this test has 127 vertical sigma-pressure hybrid layers with a model top of about 80 km and a horizontal grid spacing of about 13 km.

Control forecasts (denoted by 'ccaa05) have the same model physics as the current operational GFS; the experimental forecasts (denoted by 'ccaa41') uses the updated physics described in section 2. A comparison of the 500 hPa height anomaly correlations – which illustrate how well synoptic scale systems are represented over the globe – is shown in Fig. 8 for northern (20ºN-80ºN) and southern (20ºS-80ºS) hemispheres, and in Fig. 9 for pacific north America region (180ºE-320ºE and 20ºN-75ºN) and the entire globe for the length of the forecast. For both the northern and southern hemispheres as well as the globe, the updated physics displays significantly improved anomaly correlations for the forecast hours of 48–96-h, whereas it has a neutral impact on the 500 hPa height anomaly correlation for the forecast hours larger than 96-h. For the Pacific North America region, the anomaly correlations are significantly improved for all forecast hours of 24–144-h.

(a) Northern Hemisphere (b) Southern Hemisphere

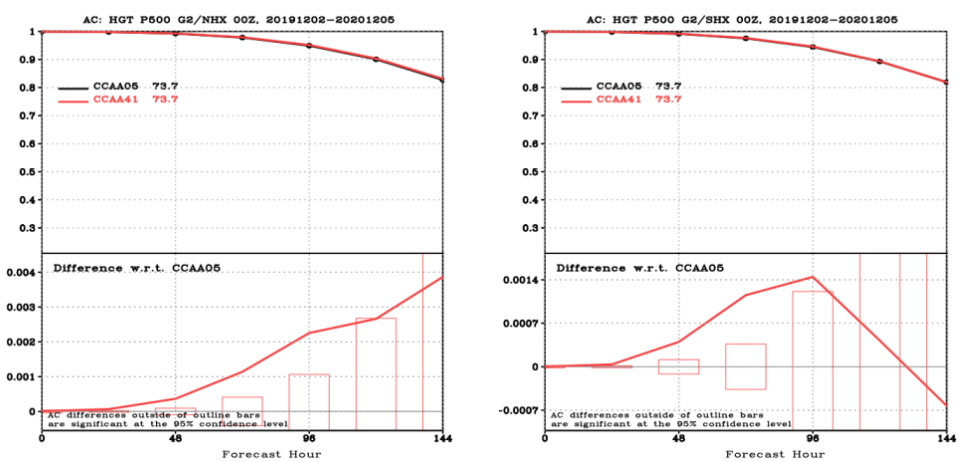

Fig. 8. Mean anomaly correlation of 500 hPa height and its difference (CCAA41 – CCAA05) for the forecasts with the updated physics (CCAA41) with respect to the control forecasts (CCAA05) in the (a) northern hemisphere (20o-80oN) and (b) southern hemisphere (20o-80oS) from 2 Dec 2019 to 5 Dec 2020. The differences outside the rectangle bars are statistically significant at the 95% confidence level.

(a) Pacific North America (b) Globe

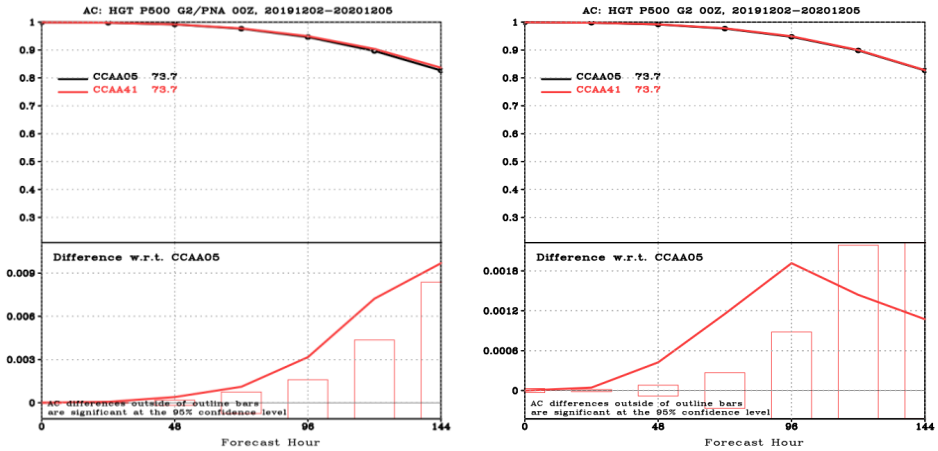

Fig. 9. As in Fig. 8, but for (a) Pacific North America and (b) globe.

Fig. 10 displays the wind vector root mean square errors (RMSE) for the tropics (20ºS-20ºN) as a function of height and forecast hour. The updated physics reduces the RMSE, especially in the troposphere, more so with increasing forecast lead time. Although not shown in Fig. 10, the updated physics displays a somewhat neutral impact on the CONUS precipitation forecast skill.

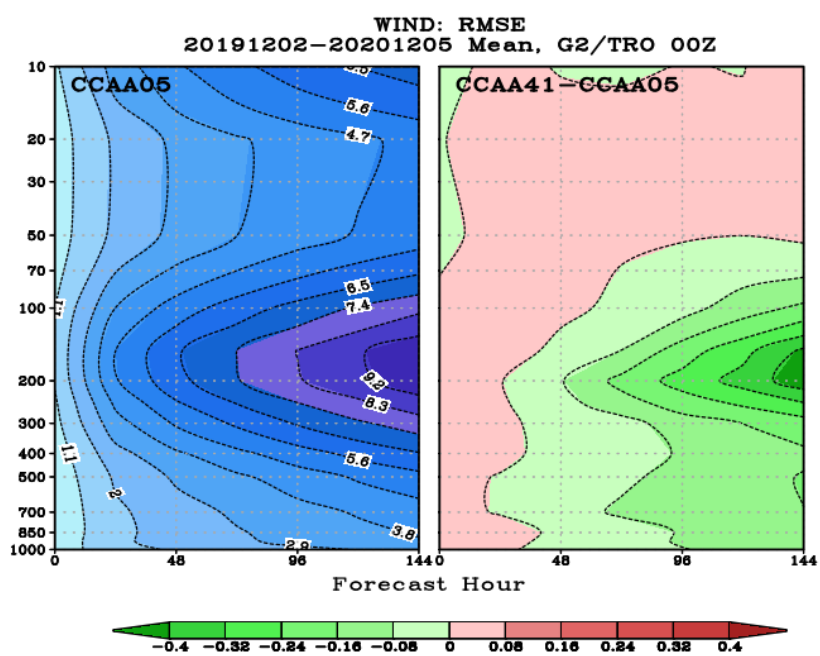

Fig. 10. Mean difference (CCAA41 – CCAA05) of wind vector RMSE over the tropics (20oS-20oN) for the forecasts with the updated physics (CCAA41) with respect to the control forecasts (CCAA05) from 2 Dec 2019 to 5 Dec 2020. Positive differences (red) are degradations and negative differences (green) are improvements.

Fig. 11 and Fig. 12 shows 2-m temperature biases over the CONUS for the summer and winter seasons, respectively. For the summer season (Fig. 11), the updated physics reduces nighttime cold biases, particularly for the CONUS East; while reductions in daytime warm biases are evident for both CONUS West and East. For the winter season (Fig. 12), the updated physics reduces nighttime warm biases for CONUS East, whereas increases in daytime temperature biases are evident for both CONUS West and East.

(a) CONUS West (b) CONUS East

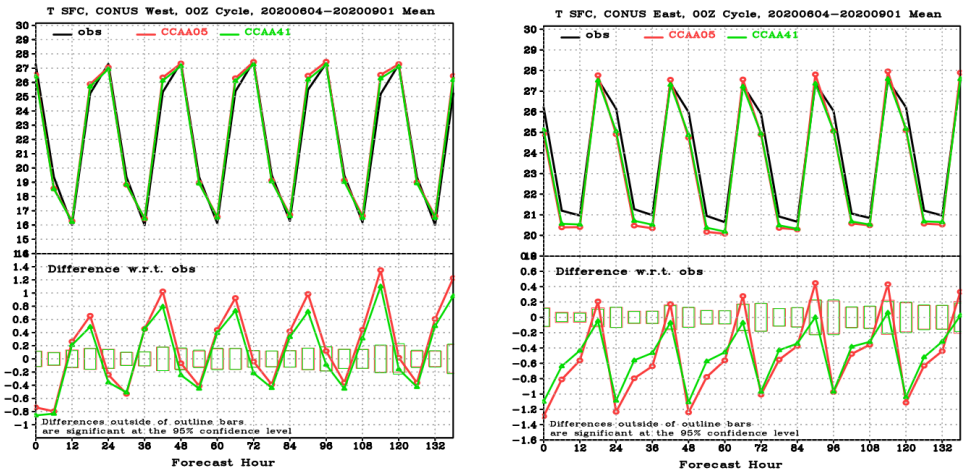

Fig. 11. Diurnal variation of 2-m temperature for the control forecasts (CCAA05) and the forecasts with the updated physics (CCAA41) with respect to the observation (obs) averaged over (a) CONUS West and (b) COUNUS East during a northern hemisphere summer season.

(a) CONUS West (b) CONUS East

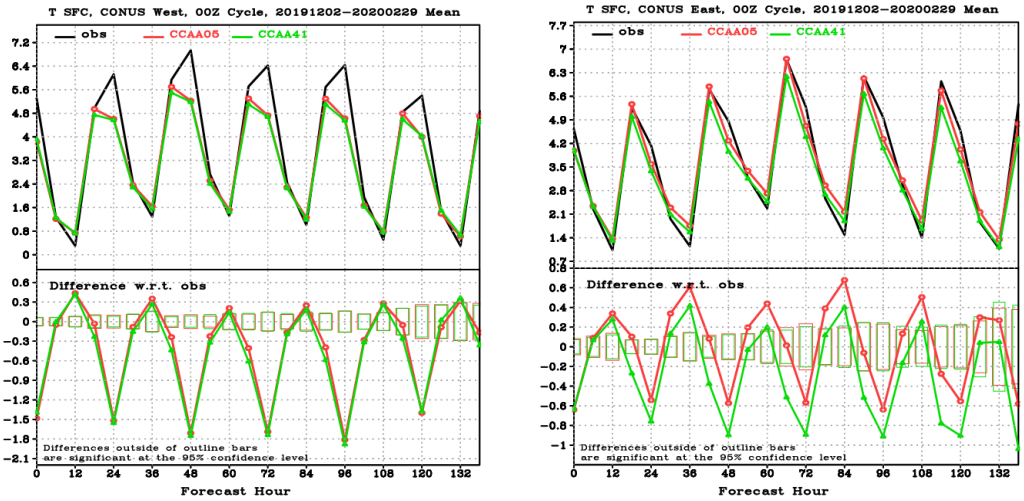

Fig. 12. As in Fig. 11, but during a northern hemisphere winter season.

For the MJO case run, a 35-day forecast run initialized on October 20, 2019 was conducted. The same GFS model and grid resolution as the medium-range forecasts were used. Although Fig. 13 shows a single case, the updated physics (denoted as 'ccbb10') improves not only the MJO intensity (Fig. 13a) but also propagation (Fig. 13b), especially for longer lead times.

(a) MJO intensity (b) MJO phase speed

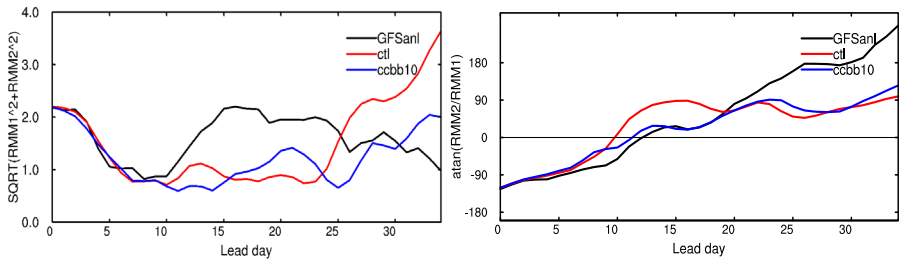

Fig. 13. (a) MJO intensity and (b) MJO phase phase speed for the control forecasts (ctl) and the forecasts with the updated physics (ccbb10) with respect to the GFS analysis (GFSanl) initialized on 20 Oct 2019. MJO intensity is defined as: $AMP = \sqrt{RMM1^2 + RMM2^2}$, MJO phase speed is defined as: $\theta = tan^{-1}(\frac{RMM2}{RMM1})$, $\theta = [-180,180]$. RMM1 and RMM2 are calculated by projecting the normalized OLR, 850 hPa and 200 hPa zonal wind anomalies averaged over 15°S-15°N to the existing MJO EOF1 and EOF2 (Wheeler and Hendon, 2004).

4. Summary

Significant updates in the GFS cumulus convection and vertical turbulent mixing schemes were made for potential implementation in the next version of the GFS (GFSv17). Stricter cumulus convection triggering conditions were applied to enhance the underestimated CAPE. Rain evaporation in cumulus convection was reduced to improve cold biases in tropospheric temperature. To reduce the excessive vertical turbulence mixing in strongly sheared environments such as that seen in hurricanes, the wind shear effect in the turbulent mixing length calculation was included. To better predict surface inversion as well as capping inversion near the PBL top, the background turbulent eddy diffusivity in the inversion layers was reduced as a function of surface roughness length and green vegetation fraction. To suppress an excessive PBL growth, the PBL updraft overshoot was limited by the bulk Richardson number-based-PBL depth.

A significant update was also made in the surface layer physics. To reduce nighttime cold and daytime warm 2m temperature biases over forested regions, a new canopy heat storage parameterization was developed. A sea spray effect parameterization was included to enhance sensible and latent heat fluxes, especially for strong wind conditions. To enhance the sensible and latent heat fluxes over the ocean, especially in weak wind conditions, molecular viscosity effect in momentum roughness length computation over ocean was also included. The new sea spray effect parameterization and increased momentum roughness length over sea in weak wind conditions helped to reduce dry biases in the PBL over the Tropics. To better represent sub-grid scale turbulence variability in the surface layer, a new parameterization for maximum surface

layer stability parameter was developed as an inverse function of the background turbulent eddy diffusivity.

The updated physics showed a significant improvement in 500-hPa height anomaly correlations for the forecast hours of 48–96-h and in the tropical wind vector root mean square errors. For CONUS East, it reduced the nighttime cold biases during summer season as well as the nighttime warm biases during winter season. In addition, the updated physics improved a Madden-Julian Oscillation intensity and propagation especially for longer lead time. The updated physics package has been ported to the NCEP GFS system for potential operational use in 2023.

Acknowledgments

The authors highly appreciate the internal reviews from Helin Wei and Qingfu Liu at the NCEP/EMC.

References

Andreas, E. L., P. O. G. Persson, and J. E. Hare, 2008: A bulk turbulent air-sea flux algorithm for high-wind, spray conditions. *J. Phys. Oceanogr.*, **38**, 1581-1596.

Beljaars, A. C. M. (1994). The parametrization of surface fluxes in large-scale models under free convection. *Quart. J. Roy. Meteor. Soc.,* **121**, 255-270.

Bougeault, P., and P. Lacarrere, 1989: Parameterization of orography-induced turbulence in a mesobeta-scale model. *Mon. Wea. Rev.*, **117**, 1872-1890.

Charnock, H., 1955: Wind stress on a water surface. *Quart. J. Roy. Meteor. Soc.,* **81**, 639-640.

Chen, F., and Y. Zhang, 2009: On the coupling strength between the land surface and the atmosphere: From viewpoint of surface exchange coefficients. *Geophys. Res. Lett.*, 36, L10404.

Fairall, C. W., J. D. Kepert, and G. J. Holland, 1994: The effect of sea spray on surface energy transports over the ocean. *Global Atmos. Ocean Syst.*, **2**, 121-142.

Garratt, J. R., 1992: *The Atmospheric Boundary Layer*. Cambridge University Press. 316 pp.

Han, J. and H.-L. Pan, 2011: Revision of Convection and Vertical Diffusion Schemes in the NCEP Global Forecast System. *Wea. and Forecasting*, **26**, 520-533.

Han, J., M. Witek, J. Teixeira, R. Sun, H.-L. Pan, J. K. Fletcher, and C. S. Bretherton, 2016: Implementation in the NCEP GFS of a hybrid eddy-diffusivity mass-flux (EDMF)

boundary layer parameterization with dissipative heating and modified stable boundary layer mixing. *Wea. and Forecasting*, **31**, 341-352.

Han, J., W. Wang, Y. C. Kwon, S.-Y. Hong, V. Tallapragada, and F. Yang, 2017: Updates in the NCEP GFS cumulus convection schemes with scale and aerosol awareness. *Wea. and Forecasting*, **32**, 2005-2017.

Han, J., and C. S. Bretherton, 2019: TKE-based moist eddy-diffusivity mass-flux (EDMF) parameterization for vertical turbulent mixing. *Wea. and Forecasting*, **34**, 869-886.

Heidkamp, M., A. Chlond, and F. Ament, 2018: Closing the energy balance using a canopy heat capacity and storage concept - a physically based approach for the land component JSBACHv3.11. *Geosci. Model Dev.*, 11, 3465–3479.

Rodier, Q., V. Masson, F. Couvreux, and A. Paci, 2017: Evaluation of a buoyancy and shear based mixing length for a turbulence scheme. *Front. Earth Sci.* 5:65.

Smith, S. D., 1988: Coefficients for sea surface wind stress, heat, and wind profiles as a function of wind speed and temperature. *J. Geophys. Res.*, **93**, 15467-15472.

Trier, S. B., M. A. Lemone, F. Chen, and K. W. Manning, 2011: Effects of surface heat and moisture exchange on ARW-WRF warm-season precipitation forecasts over the central United States. *Wea. and Forecasting*, **26**, 3-25.

Van de Wiel, B. J. H., A. F. Moene, G. J. Steeneveld, O. K. Hartogensis, and A. A. M. Holtslag, 2007: Predicting the collapse of turbulence in stably stratified boundary layers. *Flow, Turbul. Combust.*, 79, 251–274.

Wheeler, M. C., and H. H. Hendon, 2004: An all-season real-time multivariate MJO index: development of an index for monitoring and prediction. *Mon. Weather Rev.,* 132, 1917–1932.

Zheng, W., H. Wei, Z. Wang, X. Zeng, J. Meng, M. Ek, K. Mitchell, and J. Derber, 2012: Improvement of daytime land surface skin temperature over arid regions in the NCEP GFS model and its impact on satellite data assimilation. *J. Geophys. Res.*, 117, D06117.

Zheng, W., M. Ek, K. Mitchell, H. Wei, and J. Meng, 2017: Improving the stable surface layer in the NCEP global forecast system. *Mon. Wea. Rev*., **145**, 3969–3987.

Zilitinkevich, S., 1995: Non-local turbulent transport: Pollution dispersion aspects of coherent structure of convective flows. Air Pollution Theory and Simulation, H. Power, N. Moussiopoulos, and C. A. Brebbia, Eds., Vol. I, Air Pollution III, Computational Mechanics Publications, 53–60.